Check for updates

Ultrafast Science
A SCIENCE PARTNER JOURNAL

RESEARCH ARTICLE

Signature of Plasmon-Induced Hot-Electron Injection in Subpicosecond Transient Optical Response of Au-Bi:YIG Metasurface

Maxim A. Kiryanov[1], Danil A. Safiullin[1], Grigorii S. Ostanin[1], Tatyana V. Dolgova[1], Mitsuteru Inoue[2], and Andrey A. Fedyanin[1*]

[1]Faculty of Physics, Lomonosov Moscow State University, 119991 Moscow, Russia. [2]Research Institute of Electrical Communication, Tohoku University, Sendai, Miyagi 980-8577, Japan.

*Address correspondence to: fedyanin@nanolab.phys.msu.ru

We propose an approach to separate the contributions of transient solid-state processes to the ultrafast optical response of multiresonant metasurfaces. The resonant modes of a hybrid metal–dielectric metasurface based on gold nanospheres embedded in a layer of bismuth-substituted yttrium–iron garnet exhibit complex relaxation dynamics involving bulk gold, garnet, and their interface processes. Analysis of the evolution of these resonant modes makes it possible to separate the contributions of bulk and interface processes, thereby revealing the otherwise elusive plasmon-induced hot-electron transfer across the Au-Bi:YIG interface.

Citation: Kiryanov MA, Safiullin DA, Ostanin GS, Dolgova TV, Inoue M, Fedyanin AA. Signature of Plasmon-Induced Hot-Electron Injection in Subpicosecond Transient Optical Response of Au-Bi:YIG Metasurface. *Ultrafast Sci.* 2026;6:Article 0202. https://doi.org/10.34133/ultrafastscience.0202

Submitted 28 May 2026
Revised 30 July 2026
Accepted 8 September 2026
Published 16 October 2026

Copyright © 2026 Maxim A. Kiryanov et al. Exclusive licensee Xi'an Institute of Optics and Precision Mechanics. No claim to original U.S. Government Works. Distributed under a Creative Commons Attribution License (CC BY 4.0).

Introduction

Optical metasurfaces [1], which provide subwavelength engineering of the electromagnetic wave phase profile, have found wide-ranging applications in biomedicine [2], sensing [3], integrated [4] and topological [5] photonics, photovoltaics [6] and photocatalysis [7], neuromorphic [8] and analog [9] computing, nonlinear optics [10], and light control [11]. By carefully engineering the resonant modes of the metasurfaces, one can enhance and prolong light–matter interaction and achieve precise control over light scattering and absorption [12]. If there are several resonances of different types in a system, additional flexibility is available to control light in ways that extend beyond traditional photonics [13,14]. This can be realized in a multiresonant metasurface combining plasmonic and dielectric materials [15–17]. A magnetic dielectric-based metasurfaces can link photonics and spintronics within the framework of opto-spintronics [18]. In this context, bismuth-substituted yttrium iron garnet (Bi:YIG) is a particularly suitable platform for hybrid magnetophotonic metasurfaces [19], as it combines low magnetic damping with a strong magneto-optical response [20–22]. The enhanced spin-orbit coupling and tunable magnetic anisotropy in Bi:YIG enable efficient optical excitation and readout of spin dynamics, while the low magnetic damping and the possibility of growing ultrathin films make this material suitable for integration into chip-scale magnonic and spintronic circuits [22,23].

One of the key strengths of metasurfaces is the ability to change their properties on-the-fly under the influence of electric and magnetic fields or heating [24,25]. Ultrashort laser pulses make it possible to realize the light control on the subpicosecond timescale by means of different solid-state processes [26,27]. The pulses induce nonequilibrium dynamics in metals, where the heating of the electron subsystem, interactions between electrons and phonons, heat diffusion, and acoustic waves occur on femtosecond to nanosecond timescales [28–32]. In metallic nanostructures, the increase of electron and phonon temperatures leads to a modification of amplitudes and central wavelengths of plasmon resonances [33,34].

Nanostructuring itself yields additional transient effects related to quantum-size [35] and electron spill-out [36] effects, symmetry-breaking electron diffusion [37], heat-induced excitation of vibrational resonances in nanoparticles [38,39], and others. In hybrid metal–semiconductor nanostructures, the excitation of a plasmon resonance by a pump pulse induces the generation of hot electrons that can possess sufficient energy to overcome the Schottky barrier and be injected into the conduction band of the adjacent semiconductor [7,40–46]. In ferromagnetic metal/noble metal multilayer structures, ultrafast optical excitation generates hot electrons whose subsequent ballistic transport across the interface can produce spin-polarized currents, since the interfacial transmission and reflection probabilities differ for the two spin channels [47–49]. These transient processes occur simultaneously in the solid matter, can compete with each other, and exhibit different spatial localization and temporal scales. The ultrafast optical response represents a spatially averaged combination of all pump-induced perturbations to the effective dielectric permittivity, resulting in an entangled superposition of different physical mechanisms within the overall signal. One of the most common techniques for disentangling distinct ultrafast processes is broadband pump–probe spectroscopy, in which a supercontinuum probe pulse enables separate access to different processes based on their distinct spectral sensitivity [41,50,51]. However, in case

of plasmonic systems, more complex approaches may be required [33]. Hot electron and phonon nonlinearities further complicate the interpretation of the ultrafast optical response [52,53].

The plasmonic and waveguide modes in a multiresonant metasurface can respond to ultrafast perturbations in unique ways due to their distinct characteristics and different electric field spatial localization [17]. The multimodal behavior leads to diverse dynamics in the system, where the interaction timescales vary depending on the resonant modes involved [54]. In a multimodal metasurface with magnetic dielectric such as Bi:YIG, hot-electron and hot-phonon heating can be used to control magnetic dynamics on subpicosecond timescales. Ultrafast lattice heating following femtosecond laser excitation has been shown to trigger high-frequency spin waves via spin–phonon coupling in magnetic garnet films [55], and photo-induced ultrafast demagnetization has similarly been demonstrated to launch spin waves in ferrimagnetic insulators [56]. Optically guided and localized resonant modes in magnetophotonic nanostructures enable selective and tunable excitation of standing spin waves in magnetic dielectric films [57].

In this paper, we demonstrated the separation of laser-pulse-induced subpicosecond solid-state processes in a metal–dielectric optical resonant metasurface. The system of periodic gold nanospheres within Bi:YIG matrix is probed at the frequencies of plasmon and waveguide modes. We explore how the perturbation of the medium affects the dynamics of these resonant modes and distinguish processes inside metal nanoparticles and on the metal–dielectric interface. This strategy enables us to decompose the overall response into contributions from electron and phonon heating and from plasmon-induced hot-electron injection. Disentangling the ultrafast processes occurring in hybrid Au/Bi:YIG metasurfaces is a necessary prerequisite for using this platform in future work to study and control ultrafast magneto-optical phenomena such as spin-wave excitation.

Materials and Methods

The studied sample (Fig. 1A) was a hybrid metal–dielectric plasmon metasurface consisting of a two-dimensional periodic square array of gold nanospheres coated with a layer of polycrystalline bismuth-substituted yttrium iron garnet $Bi_1Y_2Fe_5O_{12}$ (Bi:YIG). The gold nanospheres had a radius of 55 nm, the array's periodicity in both directions was 600 nm, and the Bi:YIG layer had a thickness of 95 nm. The Bi:YIG layer formed hemispherical caps over the gold nanospheres with a radius of 80 nm. The sample supported various modes in the visible spectral range, including quasi-waveguide (QWG) modes and surface lattice resonances (SLRs). These modes differ in their physical origin and electromagnetic field localization. SLRs emerge from the coherent coupling of localized plasmons within the periodic array, confining the electromagnetic field primarily inside and around the gold nanospheres. Conversely, QWG modes arise from the waveguide-like propagation of a specific diffraction order within the Bi:YIG layer, with field localization predominantly within the dielectric. The transmission spectrum of the studied sample at an incidence angle of 17° exhibits several resonant features (Fig. 2, black curve): Two dips at 520 and 550 nm correspond to QWM modes, the dip at 620 nm and the peak at 670 nm are attributed to quadrupole SLRs, and the dip at 720 nm arises from the excitation of the dipole SLR. Detailed description of sample fabrication process, optical properties, and electromagnetic mode characterization can be found elsewhere [17,19].

The ultrafast measurements were conducted using a pump–probe spectroscopy technique. A regeneratively amplified titanium-sapphire laser served as a source of 70-fs pulses at a

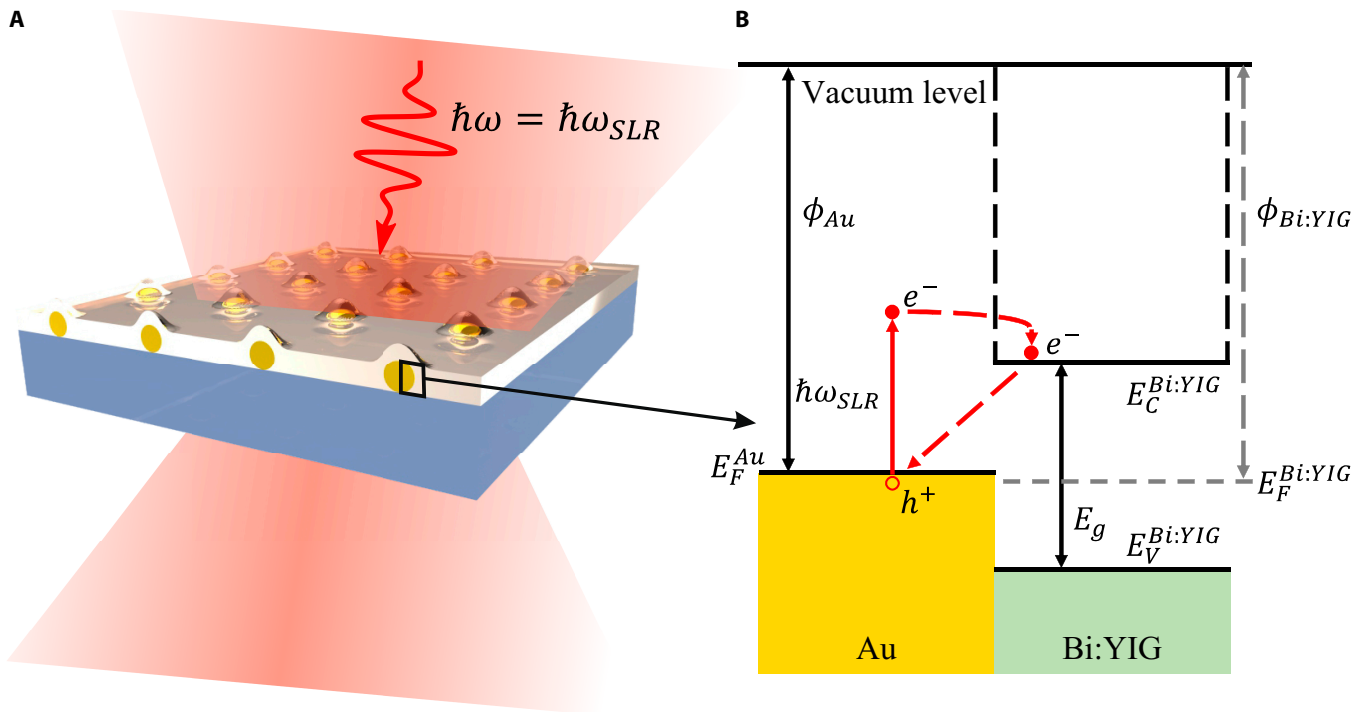


Fig. 1. (A) Scheme of the sample. (B) Schematic energy diagram of the Au/Bi:YIG interface illustrating a possible plasmon-induced hot-carrier injection process.

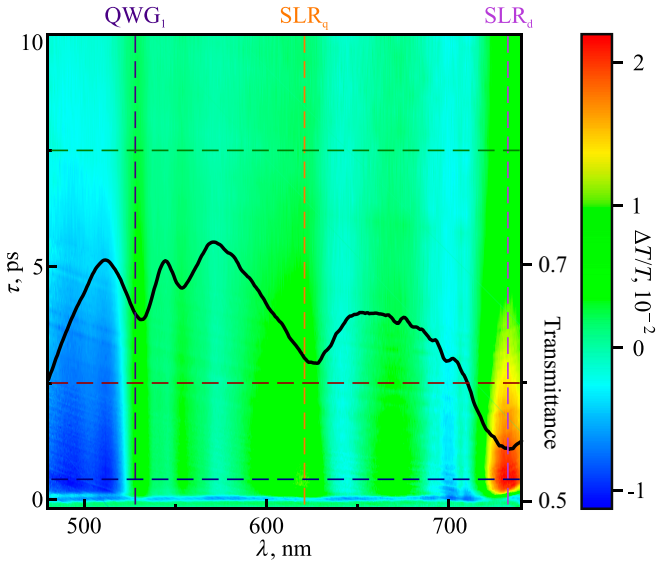


Fig. 2. Black curve: Transmittance spectrum of the Au-Bi:YIG metasurface at an incidence angle of 17°; heat map: differential transmittance dependence on wavelength λ and pump–probe time delay τ, horizontal dashed lines correspond to spectra in Fig. 3, and vertical dashed lines correspond to temporal dependences in Fig. 4.

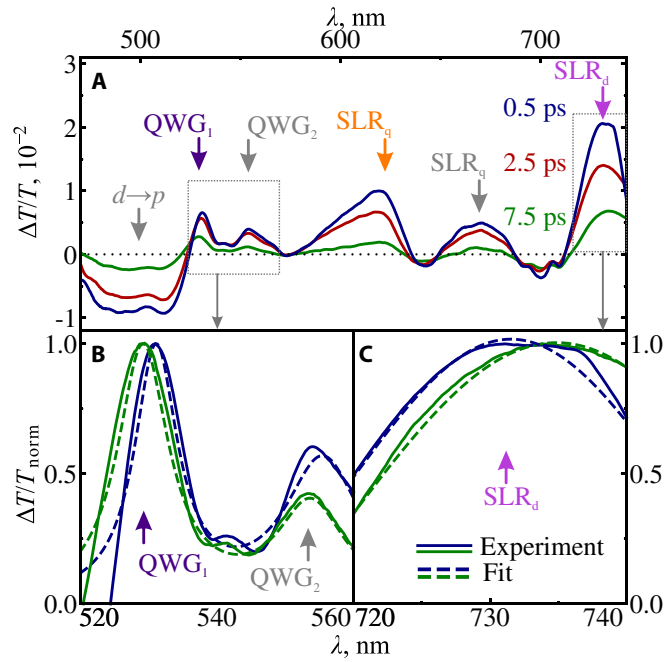


Fig. 3. (A) Experimental differential transmittance spectra $\Delta T / T(\lambda)$ at 3 time delays; arrows indicate spectral positions of the resonances. Normalized to a maximum differential transmittance spectra (solid curves) at the vicinities of the QWG modes (B) and SLR (C) and fit of the spectra (dashed curves) by Eqs. (4) (B) and (5) (C).

central wavelength of 800 nm with a repetition rate of 1 kHz. The pump pulse, with a fluence of 0.8 mJ/cm^2, was directed normally onto the sample surface, exciting the dipole SLR in the metasurface. To detect the pump-induced perturbation of the medium, a TM (transverse-magnetic)-polarized broadband supercontinuum probe pulse was used with the wavelength range spanning from 500 to 750 nm incident at an angle of 17°. Angular widths of both pump and probe beams were ≈2°. Pump and probe beams spot size diameters (full width at half maximum) were 1,000 and 200 μm, correspondingly. The probe pulse was spectrally resolved using a spectrometer, and the temporal traces were recorded at each probe wavelength. Because the supercontinuum pulse propagates through dispersive optical elements, the group velocity dispersion introduces a wavelength-dependent temporal shift, causing the pump–probe temporal overlap to shift systematically across the probe spectral range. This wavelength-dependent shift was experimentally determined and traces were subsequently corrected.

The experimentally measured value was differential transmittance, which was defined by the equation:

$$\frac{\Delta T}{T}(\tau, \lambda) = \frac{T_{pump}(\tau, \lambda) - T_0(\lambda)}{T_0(\lambda)}, \quad (1)$$

where $T_{pump}(\tau, \lambda)$ is the transmittance of the pumped sample at a given pump–probe time delay τ and probe wavelength λ, and $T_0(\lambda)$ is the transmittance of the unpumped sample.

Results

Experimental differential transmittance dependence

Differential transmittance spectra $\Delta T / T(\lambda)$ were measured at various time delays τ (Fig. 2). The transmittance modulation is observed ranging from -10^{-2} at 500 nm to 2×10^{-2} at 730 nm. The spectra show several features corresponding to different resonances (Figs. 2 and 3): the peak at 730 nm is positioned in the vicinity of dipole SLR, the peaks at 620 and 670 nm correspond to quadrupole SLRs, the peaks at 530 and 550 nm are associated with QWG modes, and the dip at 500 nm is attributed to the interband transition $d \rightarrow p$ in gold. During ≈ the first 500 fs, the peaks and the dip in $\Delta T / T(\lambda)$ spectra were increasing in amplitude and gradually decreasing at the longer timescale. The QWG-related peaks at $\lambda \simeq 530$ and 550 nm were shifting monotonically toward the blue region over time on the picosecond timescale (Fig. 3B), while the SLR-related peak at $\lambda \simeq 730$ nm was red-shifting (Fig. 3C). The $d \rightarrow p$ dip at 500 nm and the peaks in the vicinity of the plasmon modes at $\lambda \simeq 620$ and 670 nm retained their spectral positions. The fluence-dependent measurements of differential transmittance spectra $\Delta T/T(J)$ were performed at fixed time delay $\tau = 3$ ps. The results at 3 wavelengths—center of dipole SLR, 730 nm; center of the QWG mode 530 nm; blue slope of the QWG mode, 526 nm—are presented in Section S1.

The pump configuration corresponded to the excitation of the dipole SLR leading to resonant absorption of light by electron gas inside gold nanospheres. Excited electrons formed nonthermal energy distribution with the lifetime τ_{ee} (electron thermalization time) about several hundreds of femtoseconds, during which electrons thermalized to the high temperature Fermi distribution. In turn, hot electrons transferred their energy to phonons in gold on the timescale of several picoseconds τ_{ep} (electron–phonon relaxation time). These processes are thoroughly investigated in bulk gold and noble metal nanoparticles [30,38,58,59]. Nonthermal electron population, high-temperature Fermi distribution, and heated gold lattice all contribute to the modification of dielectric permittivity [59] and alter optical response of the metasurface.

Evolution of differential transmittance typical for bulk gold was observed at the wavelengths of the interband transition and in the vicinities of SLRs: after the initial growth, the absolute

value of $\Delta T / T(\tau)$ reached its maximum at a time delay of 500 fs, and picosecond relaxation was followed (Fig. 4A, violet and orange circles). Plasmonic modes and $d \rightarrow p$ transition yield different maximal values of $\Delta T / T(\tau)$ and post-relaxation levels, but qualitative temporal dependences were the same. The red-shifting of the dipole SLR-related peak at $\lambda \simeq 730$ nm did not perturb the relaxation curve.

Meanwhile, blue slopes of both QWG modes showed substantial deviation of optical transmittance evolution (Fig. 4A, dark purple circles): $\Delta T / T(\tau)$ reached maximum at longer time delays, and subsequent relaxation was suppressed. Moreover, characteristic times and qualitative temporal trends were spectrally dependent. Anomalous variation of relaxation traces with the wavelength was presented earlier [50]. Optical response evolution in the vicinity of the QWG modes is attributed to the complex interplay of the pronounced shift of the peaks in $\Delta T / T(\lambda)$ spectrum and the decrease of their amplitude.

$\Delta T / T(\tau)$ values at zero time delays at each wavelength were affected by the coherent four-wave mixing of pump and probe pulses in the Bi:YIG layer, showing itself as positive and negative extrema at the intrapulse timescale. This temporal feature was also observed in the reference flat Bi:YIG 100-nm layer (Fig. 4A, inset). Reference sample demonstrated no other temporal features indicating the absence of pump-induced solid-state processes in bulk garnet at the studied timescale.

Numerical analysis

To disentangle the different ultrafast processes in the metasurface response, a stepwise analysis is employed based on the resonant modes observed in $\Delta T / T(\lambda)$. First, the electron and lattice temperatures and carrier concentrations in gold under pump excitation are obtained, using optical calculations of the energy absorbed by a nanosphere as input. Next, we analyze and fit the resonant features associated with the plasmonic SLR and waveguide-like QWG modes. For the quadrupole SLRs, whose spectral positions remain fixed in time, these calculated temperatures are directly related to the transient amplitudes without additional spectral analysis. For the dipole SLR, the temperature dynamics are combined with a fit of the time-dependent spectral shape, while for the QWG modes, both the temperature-driven evolution and pronounced spectral shifts of the $\Delta T / T(\lambda)$ peaks are analyzed, revealing an additional, slower contribution beyond metal heating.

The electromagnetic energy of the incident pump beam was initially absorbed by electrons within gold skin layer. During the first several tens of femtoseconds, these nonthermal electrons ballistically spread deeper inside nanospheres and redistributed absorbed energy. Given that the ballistic mean free path of electrons in gold exceeds the nanosphere diameter [60,61], the absorbed energy was assumed to be uniformly distributed within the nanoparticle volume. To calculate the electron and phonon kinetics in gold, we employed the extension of the two-temperature model (eTTM)—the coupled system of the two-temperature model [28] and the rate equation [29,33,37]. This model provides the means to compute temporal dependences of the nonequilibrium electron energy density $N(\tau)$, electron temperature $\theta_e(\tau)$, and the phonon temperature $\theta_p(\tau)$:

$$\begin{cases} \dfrac{\partial N}{\partial t} = -\alpha N - \beta N + P(t) \\ \gamma \theta_e \dfrac{\partial \theta_e}{\partial t} = G\left(\theta_p - \theta_e\right) + \alpha N \\ C_p \dfrac{\partial \theta_p}{\partial t} = G\left(\theta_e - \theta_p\right) + \beta N \end{cases} \tag{2}$$

where $\alpha = 1/150\ \mathrm{fs}^{-1}$ is the average electron–electron scattering rate, $\beta = 1/1.4\ \mathrm{ps}^{-1}$ is the rate of energy transfer from the nonthermal electrons to phonons, $\gamma\theta_e = 71\ \mathrm{J\,m^{-3}\,K^{-2}}\ \theta_e$ and $C_p = 2.5 \times 10^6\ \mathrm{J\,m^{-3}\,K^{-1}}$ are electron and phonon heat capacities, $G = 2.1 \times 10^{16}\ \mathrm{W\,m^{-3}\,K^{-1}}$ is the electron–phonon coupling constant, and $P(t)$ is the heat source with a 70-fs temporal envelope, normalized so that its time and volume integral equals the energy absorbed from the pump pulse. The used constants are typical for gold [37,60]. The calculated dependences are depicted in the inset of Fig. 4B. The electron temperature reached $\theta_e \simeq 1,100$ K, while the phonon subsystem was heated up to $\theta_p \simeq 340$ K.

Next, we studied the $\Delta T / T(\lambda)$ peak associated with quadrupole SLR at $\lambda \simeq 620$ nm, the spectral position of which remains unchanged over studied time. Differential transmittance dynamics at the fixed wavelength $\Delta T / T(\tau, 620\,\mathrm{nm})$ was fitted by the combination of the calculated temporal dependences:

$$\frac{\Delta T}{T}(\tau) = a\,N(\tau) + b\,\theta_e(\tau) + c\,\theta_e^2(\tau) + d\,\theta_p(\tau), \tag{3}$$

where a, b, c, and d are fitting parameters. The quadratic dependence on θ_e is attributed to the dielectric permittivity nonlinearity at high hot-electron temperatures due to smearing of the Fermi–Dirac distribution [30]. The good agreement between the fit and the experimental data (Fig. 4B) demonstrates that the differential transmittance evolution is dictated by hot-electron dynamics in gold.

This procedure cannot be applied to the peaks associated with the QWG modes and the dipole SLR, since their spectral positions shift over time. To deduce integral temporal characteristics of each peak in the $\Delta T / T(\lambda)$ spectrum from diverse transmittance evolution, the following procedure was used. Two spectral windows were considered: the vicinity of QWG modes (520 to 560 nm) and the vicinity of the dipole SLR at the red edge of the investigated spectrum (720 to 740 nm). To numerically characterize the shape of the $\Delta T / T(\tau, \lambda)$ spectral

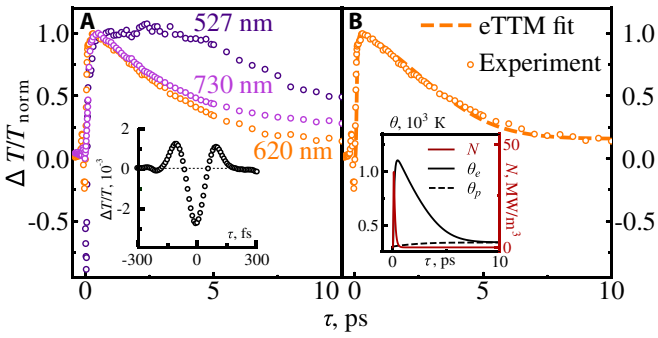


Fig. 4. (A) Experimental temporal dependences of normalized differential transmittance $\Delta T / T_{norm}(\tau)$ at the 3 wavelengths, corresponding to different resonances: 730 nm (dipole SLR, violet circles), 620 nm (quadrupole SLR, orange circles), and 527 nm (QWG mode, dark purple circles); inset depicts differential transmittance dynamics of the reference flat Bi:YIG layer. (B) Experimental dependence $\Delta T / T_{norm}(\tau)$ at 620 nm (circles) and its fit by Eq. (3) (dashed line); inset: calculated temporal dependences of nonthermalized electron energy density $N(\tau)$ (red line), temperature of thermalized electrons $\theta_e(\tau)$ (solid black line), and phonon temperature $\theta_p(\tau)$ (dashed line).

features, we approximated them by the peak functions at each time delay. The fitting procedure was conducted in the frequency domain. In the case of QWG modes, the best fit was produced by two Lorentzian functions:

$$\left.\frac{\Delta T}{T}\right|_{QWG}(\nu,\tau) = \frac{A^{QWG_1}(\tau)\left(\Delta\Gamma^{QWG_1}(\tau)\right)^2}{\left(\Delta\Gamma^{QWG_1}(\tau)\right)^2+\left(\nu-\nu_c^{QWG_1}(\tau)\right)^2} + \frac{A^{QWG_2}(\tau)\left(\Delta\Gamma^{QWG_2}(\tau)\right)^2}{\left(\Delta\Gamma^{QWG_2}(\tau)\right)^2+\left(\nu-\nu_c^{QWG_2}(\tau)\right)^2} + Bg^{QWG}(\tau), \quad (4)$$

index "1" corresponds to the bluish QWG mode peak ($\lambda \simeq 530$ nm) and index "2" corresponds to the reddish ($\lambda \simeq 550$ nm). The peak in the vicinity of SLR was approximated by Gaussian function:

$$\left.\frac{\Delta T}{T}\right|_{SLR_d}(\nu,\tau) = A^{SLR_d}(\tau)\exp\left[-\left(\frac{\nu-\nu_c^{SLR_d}(\tau)}{\Delta\Gamma^{SLR_d}(\tau)}\right)^2\right] + Bg^{SLR}(\tau). \quad (5)$$

$A^{QWG_1}(\tau), A^{QWG_2}(\tau), A^{SLR_d}(\tau)$ are the obtained amplitudes of the peaks, $\nu_c^{QWG_1}(\tau), \nu_c^{QWG_2}(\tau), \nu_c^{SLR_d}(\tau)$ are their central frequencies, and $\Delta\Gamma^{QWG_1}(\tau), \Delta\Gamma^{QWG_2}(\tau), \Delta\Gamma^{SLR_d}(\tau)$ are peak widths. $Bg^{QWG}(\tau)$ and $Bg^{SLR}(\tau)$ are constant background terms that are nonzero only at time delays where the pump and probe pulses temporally overlap, arising from coherent four-wave mixing.

In the spectral vicinity of the dipole SLR, the resonance originates from the coupling between the single-particle plasmon and a narrow diffraction anomaly whose central wavelength is strongly angle-dependent. The measured linewidth is therefore governed by the angular dispersion of the lattice mode convolved with the finite angular spread of the probe beam, which yields an effectively Gaussian envelope. In contrast, the QWG modes spectral position is set mainly by the Bi:YIG layer thickness and refractive index, and their spectral profile is well approximated by the standard Lorentzian response of a resonant lineshape.

The evolution of the peak amplitudes $A^{QWG_1}(\tau), A^{SLR_d}(\tau)$ and central wavelengths $\lambda_c^{QWG_1}(\tau), \lambda^{SLR_d}(\tau)$ is presented in Fig. 4 (circles). Temporal dependences of $A^{QWG_2}(\tau)$ and $\lambda_c^{QWG_2}(\tau)$ for the reddish QWG mode qualitatively matched the dynamics of the bluish QWG mode. Dipole SLR peak's amplitude dynamics $A^{SLR_d}(\tau)$ displays typical exponential relaxation, while $\lambda^{SLR_d}(\tau)$ dependence shows fast and subsequent slow excitation. In case of QWG, both $A^{QWG_1}(\tau)$ and $\lambda_c^{QWG_1}(\tau)$ demonstrate retarded relaxation, which clearly indicates the existence of additional slower processes. The same peak analysis was conducted for fluence-dependent measurements of differential transmittance spectra; the results can be found in Section S2. Temporal dependence of peak widths $\Delta\Gamma^{QWG_1}$ and $\Delta\Gamma^{SLR_d}$ are presented in Section S3.

Further, we applied the eTTM fitting procedure to the obtained $A^{SLR_d}(\tau)$ and $\lambda_c^{SLR_d}(\tau)$ dependences, analogous to Eq. (3):

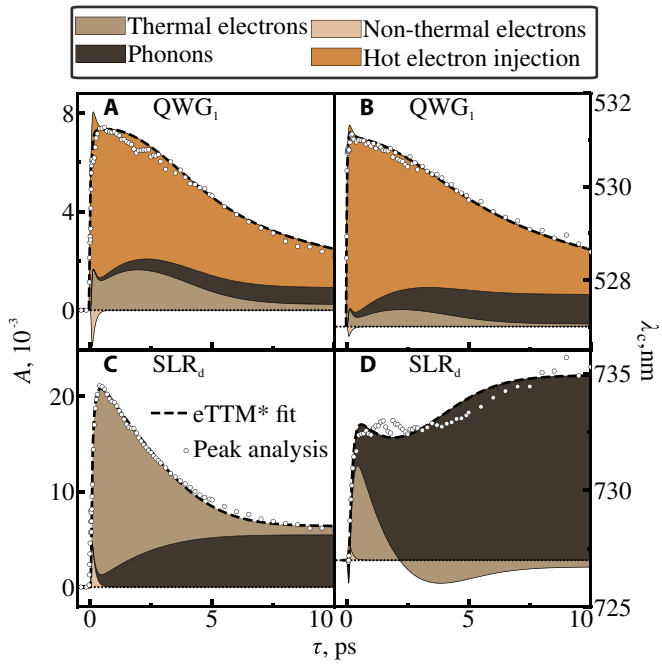


Fig. 5. The temporal dependences of $\Delta T / T(\lambda)$ peak amplitudes $A(\tau)$ (A and C) and their central wavelengths $\lambda(\tau)$ (B and D); circles represent the data obtained from the peak analysis of the experimental spectra by Eqs. (4) and (5); dashed lines correspond to the fits to these data by eTTM* [Eq. (7) for A and B and Eq. (6) for C and D]; (A) and (B) correspond to the analysis of the vicinity the bluish QWG mode, and (C) and (D) correspond to the dipole SLR. The area of the colored regions corresponds to the impacts of the different summands in Eqs. (6) and (7) to the overall dynamics.

$$A^{SLR_d}(\tau) = a\,N(\tau) + b\,\theta_e(\tau) + c\,\theta_e^2(\tau) + d\,\theta_p(\tau),$$
$$\lambda_c^{SLR_d}(\tau) = \Lambda_0 + a\,N(\tau) + b\,\theta_e(\tau) + c\,\theta_e^2(\tau) + d\,\theta_p(\tau), \quad (6)$$

where a, b, c, d, and Λ_0 are fitting parameters. The sets of fitting parameters were selected independently for each curve. Functions $N(\tau), \theta_e(\tau)$, and $\theta_p(\tau)$ corresponded to the same solution of eTTM [Eq. (2)] as in Eq. (3). Peak amplitude and central wavelength dynamics were reproduced by electron and phonon evolution (Fig. 5C and D, dashed lines). The beige area in Fig. 5 corresponds to the impact of the nonthermal electrons in the overall dynamics [$aN(\tau)$ summand], the sandy-colored area displays the impact of the thermal electrons, and the dark brown area represents the impact of the phonon temperature. The slow excitation in Fig. 5D is described by temperature dynamic in gold and attributed to the substantial impact of the rising phonon temperature.

However, the same fitting procedure fails to reproduce the retarded relaxation in the case of QWG modes. To describe $A^{QWG_1}(\tau)$ and $\lambda_c^{QWG_1}(\tau)$ dependences, we modify eTTM by adding an exponentially decaying summand to Eq. (6) (eTTM* fit):

$$A^{QWG_1}(\tau) = a\;N(\tau) + b\;\theta_e(\tau) + c\;\theta_e^2(\tau) + d\;\theta_p(\tau) + \left[f\exp\left(-\frac{\tau}{\tilde{\tau}}\right)H(\tau)\right] \otimes \exp\left(-\frac{\tau^2}{\tau_{pump}^2}\right),$$
$$\lambda_c^{QWG_1}(\tau) = \Lambda_0 + a\;N(\tau) + b\;\theta_e(\tau) + c\;\theta_e^2(\tau) + d\;\theta_p(\tau) + \left[f\exp\left(-\frac{\tau}{\tilde{\tau}}\right)H(\tau)\right] \otimes \exp\left(-\frac{\tau^2}{\tau_{pump}^2}\right), \quad (7)$$

where Gaussian function corresponds to the temporal envelope of the pump pulse, the Heaviside step function $H(\tau)$ limits the exponents grow at negative times, and f and $\tilde{\tau}$ are fitting parameters, alongside with a, b, c, d, and Λ_0 As previously mentioned, the sets of fitting parameters were selected independently and the functions $N(\tau)$, $\theta_e(\tau)$, and $\theta_p(\tau)$ corresponded to the same solution of the eTTM [Eq. (2)]. Results of the fit with $\tilde{\tau} \approx 7$ ps are shown in Fig. 4A and B (dashed line). The contribution of the additional term to the overall dynamics (brown area in Fig. 4A and B) considerably exceeds that of the processes occurring inside gold. At the same time, applying the eTTM* fit to $A^{SLR_d}(\tau)$ and $\lambda_c^{SLR_d}(\tau)$ dependences instead of Eq. (6) results in either the relaxation constant $\tilde{\tau}$ approaching the electron–phonon relaxation time ~3 ps or the amplitude of the term f becoming negligibly small depending on initial conditions.

Analyzing the spectral vicinity of the plasmonic resonances alone does not allow the additional process to be resolved, because the hot-carrier injection produces only a weak signature there compared to the dominant dynamics in gold. At the same time, this plasmonic window provides a way to determine and fix the parameters of the electron and lattice dynamics in gold, which are then used in the analysis of the temporal traces in the spectral vicinity of the QWG mode. In contrast, examining only the QWG spectral region requires a fitting procedure with several exponential contributions with close characteristic times, which does not yield a reliable description of the dynamics. A comprehensive depiction of the solid-state processes in the hybrid metasurface can therefore be obtained by considering the plasmon and QWG modes together.

Discussion

Comparing the dynamics of $A^{SLR_d}(\tau)$, $\lambda_c^{SLR_d}(\tau)$ and $A^{QWG_1}(\tau)$, $\lambda_c^{QWG_1}(\tau)$ and taking into account the spectral independence of electron–phonon relaxation time [30,58], the additional decaying term cannot be attributed to the hot electron dynamics inside gold nanospheres and corresponds to a parallel process with characteristic time of ~ 7 ps. Excitation of any vibrational resonances of gold nanoparticles [38] or acoustic waves inside the garnet layer [62] should occur on a considerably longer timescale. Pumping the reference Bi:YIG layer displays only coherent four-wave mixing without any prolonged perturbation. Since the observed additional process cannot be referred to the gold nanoparticles and garnet layer separately, we associate it with the gold–garnet interface.

A possible explanation is the plasmon-induced injection of hot carriers across the Au/Bi:YIG interface (Fig. 1B). Bi:YIG exhibits a band gap with an upper estimation of $E_g \lesssim 2.6$ eV [20,21,63] (transition at the tetrahedral iron site), which is responsible for its magneto-optical activity; a typical work function for transition-metal oxides, a class that includes Bi:YIG, is $\phi_{Bi:YIG} \approx 4.9$ eV [64]; the work function of gold is $\phi_{Au} \approx 4.8$ eV [65]. Therefore, the Schottky-like energy barrier between the Fermi level of gold and Bi:YIG conduction band can be estimated as $E_C^{Bi:YIG} - E_F^{Au} \approx 1.2$ eV. In turn, the pump pulse spectrally corresponds to the excitation of SLR and is resonantly absorbed by Au spheres. Therefore, at the initial stage, a part of the electron population coherently oscillates and has an excess energy of 1.5 eV above the Fermi level. This energy is high enough to overcome the interfacial barrier, and some of these hot electrons can be transferred from Au into empty states of Bi:YIG conduction band before plasmon oscillation stops. In this process, holes remain in Au, so the interface temporarily acquires a charge-separated character. In our case, we consider the effective decay time of the interfacial perturbation to be ≈ 7 ps. Such hot-carrier transfer is known in metal/semiconductor interfaces and related hybrid systems as an ultrafast process occurring on femtosecond to picosecond timescales and capable of producing transient changes in optical properties [7,40–46]. In the Au/Bi:YIG structure, this mechanism can lead to a transient redistribution of charge and occupation of electronic states near the interface, which modifies the local dielectric response and, consequently, affects the optical signal measured in the pump–probe experiment. Because the conduction band of Bi:YIG is intrinsically spin-split by the exchange interaction, the density of empty states available to accept an injected hot electron differs between the two spin channels once the sample carries a net magnetization. This asymmetry should provide the spin-selective plasmon-induced hot-electron injection, opening a new route toward all-optical, pump-induced spin injection into a magnetic oxide.

In conclusion, we suggest a method to distinguish the impacts of transient solid-state processes on the ultrafast optical response of multiresonant metasurfaces. By analyzing the evolution of different resonant modes in a multiresonant metasurface, the contributions of processes occurring in the bulk and at the metal–dielectric interface are separated. The dynamics of the plasmonic modes primarily reflects processes inside gold nanospheres. Examining the evolution of waveguide mode reveals the existence of the plasmon-induced hot-carriers injection across the Au-Bi:YIG interface. This opens up a new regime of magnetic perturbation on the picosecond timescale, with potential applications in spintronics and ultrafast magnetism.

Acknowledgments

Funding: This work was financially supported by the Russian Science Foundation, project no. 24-12-00210. Equipment provided by the MSU development program (nos. 102-14.02.2022 and 2-10.10.2025-13-06.04.2020) was used in the experiment.
Author contributions: All authors contributed equally to the writing of the manuscript.
Competing interests: The authors declare that they have no competing interests.

Data Availability

The data that support the findings of this study are available from the corresponding author upon reasonable request.

Supplementary Materials

Section S1 to S3

References

1. Kuznetsov AI, Brongersma ML, Yao J, Chen MK, Levy U, Tsai DP, Zheludev NI, Faraon A, Arbabi A, Yu N, et al. Roadmap for optical metasurfaces. *ACS Photonics*. 2024;11(3):816–865.
2. Kim H, Yun H, Jeong S, Lee S, Cho E, Rho J. Optical metasurfaces for biomedical imaging and sensing. *ACS Nano*. 2025;19(3):3085–3114.

3. Ray D, Raziman TV, Santschi C, Etezadi D, Altug H, Martin OJF. Hybrid metal-dielectric metasurfaces for refractive index sensing. *Nano Lett*. 2020;20(12):8752–8759.
4. Wang Z, Xiao Y, Liao K, Li T, Song H, Chen H, Uddin SMZ, Mao D, Wang F, Zhou Z, et al. Metasurface on integrated photonic platform: From mode converters to machine learning. *Nanophotonics*. 2022;110(16):3531–3546.
5. Ustinov AS, Shorokhov AS, Smirnova DA. Topological photonics (brief review). *JETP Lett*. 2021;114(12):719–728.
6. Mascaretti L, Chen Y, Henrotte O, Yesilyurt O, Shalaev VM, Naldoni A, Boltasseva A. Designing metasurfaces for efficient solar energy conversion. *ACS Photonics*. 2023;10(12):4079–4103.
7. Jia H, Tso CC, Abed AE, Yu W, Jian A, Sang S, Zhang X. Metallic plasmonic nanostructure arrays for enhanced solar photocatalysis. *Laser Photonics Rev*. 2023;17(5):2200700.
8. Wu C, Yu H, Lee S, Peng R, Takeuchi I, Li M. Programmable phase-change metasur faces on waveguides for multimode photonic convolutional neural network. *Nat Commun*. 2021;12(1):96.
9. Yushkov VV, Sitnyansky VA, Shorokhov AS, Fedyanin AA. Analog optical correlation augmented by Mie-resonant metasurfaces. *ACS Photonics*. 2024;11(6):2506–2512.
10. Nazarenko AA, Chernyak AM, Musorin AI, Shorokhov AS, Ding L, Valuckas V, Nonahal M, Aharonovich I, Ha ST, Kuznetsov AI, et al. Cryogenic nonlinear microscopy of high-Q metasurfaces coupled with transition metal dichalcogenide monolayers. *Nanophotonics*. 2024;13(18): 3429–3436.
11. Abdollahramezani S, Hemmatyar O, Taghinejad M, Taghinejad H, Kiarashinejad Y, Zandehshahvar M, Fan T, Deshmukh S, Eftekhar AA, Cai W, et al. Dynamic hybrid metasurfaces. *Nano Lett*. 2021;21(3):1238–1245.
12. Kolkowski R, Berkhout A, Roscam Abbing SDC, Pal D, Dieleman CD, Geuchies JJ, Houtepen AJ, Ehrler B, Koenderink AF. Temporal dynamics of collective resonances in periodic metasurfaces. *ACS Photonics*. 2024;11(6):2480–2496.
13. Reshef O, Saad-Bin-Alam M, Huttunen MJ, Carlow G, Sullivan BT, Ménard J-M, Dolgaleva K, Boyd RW. Multiresonant high-Q plasmonic metasurfaces. *Nano Lett*. 2019;9(9):6429–6434.
14. Taghinejad M, Taghinejad H, Malak ST, Moradinejad H, Woods EV, Xu Z, Liu Y, Eftekhar AA, Lian T, Tsukruk VV, et al. Sharp and tunable crystal/fano-type resonances enabled by out-of-plane dipolar coupling in plasmonic nanopatch arrays. *Ann Phys*. 2018;530(10):1700395.
15. Barreda Á, Vitale F, Minovich AE, Ronning C, Staude I. Applications of hybrid metal-dielectric nanostructures: State of the art. *Adv Photonics Res*. 2022;3(4):2100286.
16. Henriksson N, Gabbani A, Petrucci G, Garoli D, Pineider F, Maccaferri N. Probing temperature changes using nonradiative processes in hyperbolic meta-antennas. *ACS Appl Opt Mater*. 2024;2(12):2469–2475.
17. Musorin AI, Chetvertukhin AV, Dolgova TV, Uchida H, Inoue M, Luk'Yanchuk BS, Fedyanin AA. Tunable multimodal magnetoplasmonic metasurfaces. *Appl Phys Lett*. 2019;115(15):151102.
18. Němec P, Fiebig M, Kampfrath T, Kimel AV. Antiferromagnetic opto-spintronics. *Nat Phys*. 2018;14(3):229–241.
19. Chetvertukhin AV, Musorin AI, Dolgova TV, Uchida H, Inoue M, Fedyanin AA. Transverse magneto-optical Kerr effect in 2D gold–garnet nanogratings. *J Magn Magn Mater*. 2015;383:110–113.
20. Dionne GF. *Magnetic oxides*. Boston (MA): Springer US; 2009.
21. Deb M, Popova E, Fouchet A, Keller N. Magneto-optical faraday spectroscopy of completely bismuth-substituted $Bi_3Fe_5O_{12}$ garnet thin films. *J Phys D Appl Phys*. 2012;45(45):455001.
22. Wang H, Legrand W, Petrosyan D, Kang M-G, Karadža E, Matsumoto H, Schlitz R, Lammel M, Aguirre MH, Gambardella P. Ultrathin bismuth-yttrium iron garnet films with tunable magnetic anisotropy. *Phys Rev Mater*. 2026;10(3):034404.
23. Serga AA, Chumak AV, Hillebrands B. YIG magnonics. *J Phys D Appl Phys*. 2010;43(26):264002.
24. Li T, Xu H, Panmai M, Shao T, Gao G, Xu F, Hu G, Wang S, Wang Z, Zhu S. Ultrafast metaphotonics. *Ultrafast Sci*. 2024;4:0074.
25. Maiuri M, Schirato A, Cerullo G, Della Valle G. Ultrafast all-optical metasurfaces: Challenges and new frontiers. *ACS Photonics*. 2024;11(8):2888–2905.
26. Iqbal MA, Lin W, Pengyun W, Qiu J, Liu X. Ultrafast plasmonics for all-optical switching and pulsed lasers. *Ultrafast Sci*. 2024;4:0048.
27. Koya AN, Romanelli M, Kuttruff J, Henriksson N, Stefancu A, Grinblat G, De Andres, Schnur F, Vanzan M, Marsili M, et al. Advances in ultrafast plasmonics. *Appl Phys Rev*. 2023;10(2):021318.
28. Anisimov SI, Kapeliovich BL, T. L. Perel'man. Electron emission from metal surfaces exposed to ultrashort laser pulses. *J Exp Theor Phys*. 1974;39(2):375–377.
29. Sun C-K, Vallée F, Acioli LH, Ippen EP, Fujimoto JG. Femtosecond-tunable measurement of electron thermalization in gold. *Phys Rev B*. 1994;50(20):15337–15348.
30. Besteiro LV, Yu P, Wang Z, Holleitner AW, Hartland GV, Wiederrecht GP, Govorov AO. The fast and the furious: Ultrafast hot electrons in plasmonic metastructures. Size and structure matter. *Nano Today*. 2019;27:120–145.
31. Block A, Liebel M, Yu R, Spector M, Sivan Y, García De Abajo FJ, Van Hulst. Tracking ultrafast hot-electron diffusion in space and time by ultrafast thermomodulation microscopy. *Sci Adv*. 2019;(5):5:eaav8965.
32. Khokhlov VA, Romashevskiy SA, Ashitkov SI, Inogamov NA. Synchronous detection of nonlinear phenomena in opto-acoustic vibrations induced in a nanofilm by a femtosecond laser pulse. *JETP Lett*. 2024;120(7):531–539.
33. Schirato A, Silva MG, Teles-Ferreira DC, Manzoni C, De Paula, Cerullo G, Della Valle G, Di Vece. Disentangling the ultrafast nonlinear optical behavior of plasmonic resonances near the interband transition. *Adv Photonics Res*. 2023;4(1):2200081.
34. Dong X, He Y, Gao R, Yang K, Wang J, Yang W, Li J, Ren B, Li M-D, Yang Z. Plasmonic ultrafast all-optical switching with a superior on–off ratio. *Nano Lett*. 2025;25(10):4005–4012.
35. Lermé J. Size evolution of the surface plasmon resonance damping in silver nanoparticles: Confinement and dielectric effects. *J Phys Chem C*. 2011;115(29):14098–14110.
36. Avdizhiyan A, Janus W, Szpytma M, Ślezak T, Przybylski M, Chrobak M, Roddatis V, Stupakiewicz A, Razdolski I. Ultrafast laser-induced dynamics of non-equilibrium electron spill-out in nanoplasmonic bilayers. *Nano Lett*. 2024;24(1):466–471.
37. Schirato A, Maiuri M, Toma A, Fugattini S, Proietti Zaccaria R, Laporta P, Nordlander P, Cerullo G, Alabastri A, Della Valle G. Transient optical symmetry breaking for ultrafast broadband dichroism in plasmonic metasurfaces. *Nat Photonics*. 2020;14(12):723–727.

38. Hartland GV. Optical studies of dynamics in noble metal nanostructures. *Chem Rev*. 2011;111(6):3858–3887.
39. Cunha J, Guo T-L, Della Valle G, Koya AN, Proietti Zaccaria R, Alabastri A. Controlling light, heat, and vibrations in plasmonics and phononics. *Adv Opt Mater*. 2020;8(24):2001225.
40. Wu K, Chen J, McBride JR, Lian T. Efficient hot-electron transfer by a plasmon induced interfacial charge-transfer transition. *Science*. 2015;349(6248):632–635.
41. Taghinejad M, Taghinejad H, Xu Z, Lee K-T, Rodrigues SP, Yan J, Adibi A, Lian T, Cai W. Ultrafast control of phase and polarization of light expedited by hot-electron transfer. *Nano Lett*. 2018;18(9):5544–5551.
42. Liu Y, Chen Q, Cullen DA, Xie Z, Lian T. Efficient hot electron transfer from small au nanoparticles. *Nano Lett*. 2020;20(6):4322–4329.
43. Jia H, Li Z, Wang B, Xing G, Wong YL, Ren H, Li M, Wong K-Y, Lei D, Wong L-W, et al. Plasmonic nanohole arrays with enhanced visible light photoelectrocatalytic activity. *ACS Photonics*. 2022;9(2):652–663.
44. Zhou L, Huang Q, Xia Y. Plasmon-induced hot electrons in nanostructured materials: Generation, collection, and application to photochemistry. *Chem Rev*. 2024;124(14):8597–8619.
45. Tagliabue G, DuChene JS, Abdellah M, Habib A, Gosztola DJ, Hattori Y, Cheng W-H, Zheng K, Canton SE, Sundararaman R, et al. Ultrafast hot-hole injection modifies hot-electron dynamics in Au/p-GaN heterostructures. *Nat Mater*. 2020;19(12):1312–1318.
46. Sortino L, Guimarães MH, Molina-Sánchez A, Quan J, Garoli D, Maccaferri N. Light-matter interactions in layered materials and heterostructures: From moiré physics and magneto-optical effects to ultrafast dynamics and hybrid meta-photonics. *2D Mater*. 2025;12(3):033003.
47. Melnikov A, Brandt L, Liebing N, Ribow M, Mertig I, Woltersdorf G. Ultrafast spin transport and control of spin current pulse shape in metallic multilayers. *Phys Rev B*. 2022;106(10):104417.
48. Elliott P, Eschenlohr A, Chen J, Shallcross S, Bovensiepen U, Dewhurst JK, Sharma S. Transient spin injection efficiencies at ferromagnet–metal interfaces. *Adv Mater Interfaces*. 2022;9(36):2201233.
49. Lu W-T, Yuan Z, Xu X. Ultrafast magnetization enhancement and spin current injection in magnetic multilayers by exciting the nonmagnetic metal. *Sci China Phys Mech Astron*. 2023;66(12):127511.
50. Jani H, Duan L. Time-frequency spectroscopy of GaAs transient dispersion using few-cycle pump-probe reflectometry. *Phys Rev Appl*. 2020;13(5):054010.
51. Yeh T-T, Shirai H, Tu C-M, Fuji T, Kobayashi T, Luo C-W. Ultrafast carrier dynamics in Ge by ultra-broadband mid-infrared probe spectroscopy. *Sci Rep*. 2017;7(1):40492.
52. Schirato A, Crotti G, Silva MG, Teles-Ferreira DC, Manzoni C, Proietti Zaccaria R, Laporta P, De Paula, Cerullo G, Della Valle G. Ultrafast plasmonics beyond the perturbative regime: Breaking the electronic-optical dynamics correspondence. *Nano Lett*. 2022;22(7):2748–2754.
53. Kiryanov MA, Novikov IA, Frolov AY, Dolgova TV, Fedyanin AA. Surface plasmon-assisted control of ultrafast optical relaxation traces. *Laser Photonics Rev*. 2025;19(17):2500053.
54. Kiryanov MA, Ostanin GS, Dolgova TV, Inoue M, Fedyanin AA. Anomalous picosecond optical transmittance dynamics in Au-Bi:YIG hybrid metasurface. *JETP Lett*. 2023;117(3):196–201.
55. Deb M, Popova E, Zeuschner SP, Hehn M, Keller N, Mangin S, Malinowski G, Bargheer M. Generation of spin waves via spin-phonon interaction in a buried dielectric thin film. *Phys Rev B*. 2021;103(2):024411.
56. Hashimoto Y, Daimon S, Iguchi R, Oikawa Y, Shen K, Sato K, Bossini D, Tabuchi Y, Satoh T, Hillebrands B, et al. All-optical observation and reconstruction of spin wave dispersion. *Nat Commun*. 2017;8(1):15859.
57. Chernov AI, Kozhaev MA, Ignatyeva DO, Beginin EN, Sadovnikov AV, Voronov AA, Karki D, Levy M, Belotelov VI. All-dielectric nanophotonics enables tunable excitation of the exchange spin waves. *Nano Lett*. 2020;20(7):5259–5266.
58. Chiang W-Y, Bruncz A, Ostovar B, Searles EK, Brasel S, Hartland G, Link S. Electron–phonon relaxation dynamics of hot electrons in gold nanoparticles are independent of excitation pathway. *J Phys Chem C*. 2023;127(43):21176–21185.
59. Stoll T, Maioli P, Crut A, Del Fatti, Vallée F. Advances in femto-nano-optics: Ultrafast nonlinearity of metal nanoparticles. *Eur Phys J B*. 2014;87(11):50515.
60. Wellershoff S-S, Hohlfeld J, Güdde J, Matthias E. The role of electron–phonon coupling in femtosecond laser damage of metals. *Appl Phys A Mater Sci Process*. 1999;69(S1):S99–S107.
61. Karna P, Hoque MSB, Thakur S, Hopkins PE, Giri A. Direct measurement of ballistic and diffusive electron transport in gold. *Nano Lett*. 2023;23(2):491–496.
62. Deb M, Popova E, Hehn M, Keller N, Mangin S, Malinowski G. Picosecond acoustic excitation-driven ultrafast magnetization dynamics in dielectric bi-substituted yttrium iron garnet. *Phys Rev B*. 2018;98(17):174407.
63. Li W-K, Guo G-Y. First-principles study on magneto-optical effects in the ferromagnetic semiconductors $Y_3Fe_5O_{12}$ and $Bi_3Fe_5O_{12}$. *Phys Rev B*. 2021;103(1):014439.
64. Rietwyk KJ, Keller DA, Ginsburg A, Barad H-N, Priel M, Majhi K, Yan Z, Tirosh S, Anderson AY, Ley L, et al. Universal work function of metal oxides exposed to air. *Adv Mater Interfaces*. 2019;6(12):1802058.
65. Anderson PA. Work function of gold. *Phys Rev*. 1959;115(3):553–554.

Ultrafast Science
A SCIENCE PARTNER JOURNAL

Signature of Plasmon-Induced Hot-Electron Injection in Subpicosecond Transient Optical Response of Au-Bi:YIG Metasurface

Maxim A. Kiryanov, Danil A. Safiullin, Grigorii S. Oŝtanin, Tatyana V. Dolgova, Mitsuteru Inoue, and Andrey A. Fedyanin

Citation: Kiryanov M, Safiullin D, Ostanin G, Dolgova T, Inoue M, Fedyanin A. Signature of Plasmon-Induced Hot-Electron Injection in Subpicosecond Transient Optical Response of Au-Bi:YIG Metasurface. *Ultrafast Sci*. 2026;**6**:0202. DOI: 10.34133/ultrafastscience.0202

We propose an approach to separate the contributions of transient solid-state processes to the ultrafast optical response of multiresonant metasurfaces. The resonant modes of a hybrid metal–dielectric metasurface based on gold nanospheres embedded in a layer of bismuth-substituted yttrium–iron garnet exhibit complex relaxation dynamics involving bulk gold, garnet, and their interface processes. Analysis of the evolution of these resonant modes makes it possible to separate the contributions of bulk and interface processes, thereby revealing the otherwise elusive plasmon-induced hot-electron transfer across the Au-Bi:YIG interface.
Image

View the article online
https://spj.science.org/doi/10.34133/ultrafastscience.0202

Use of this article is subject to the Terms of service

Ultrafast Science (ISSN 2765-8791) is published by the American Association for the Advancement of Science. 1200 New York Avenue NW, Washington, DC 20005.

Copyright © 2026 Maxim A. Kiryanov et al.

Exclusive licensee Xi'an Institute of Optics and Precision Mechanics. No claim to original U.S. Government Works. Distributed under a Creative Commons Attribution License (CC BY 4.0).